Ultra-High-Resolution Coronary CT Angiography With Photon-Counting Detector CT

Feasibility and Image Characterization

Victor Mergen, MD, Thomas Sartoretti, BMed,*†‡ Matthias Baer-Beck, PhD,§ Bernhard Schmidt, PhD,§ Martin Petersilka, PhD,§ Joachim Ernst Wildberger, MD, PhD,†‡ André Euler, MD,* Matthias Eberhard, MD, EBCR,* and Hatem Alkadhi, MD, MPH, EBCR, FESER**

Objectives: The aim of this study was to evaluate the feasibility and quality of ultra-high-resolution coronary computed tomography angiography (CCTA) with dual-source photon-counting detector CT (PCD-CT) in patients with a high coronary calcium load, including an analysis of the optimal reconstruction kernel and matrix size.

Materials and Methods: In this institutional review board–approved study, 20 patients (6 women; mean age, 79 ± 10 years; mean body mass index, 25.6 ± 4.3 kg/m^2) undergoing PCD-CCTA in the ultra-high-resolution mode were included. Ultra-high-resolution CCTA was acquired in an electrocardiography-gated dual-source spiral mode at a tube voltage of 120 kV and collimation of 120 × 0.2 mm. The field of view (FOV) and matrix sizes were adjusted to the resolution properties of the individual reconstruction kernels using a FOV of 200 × 200 mm^2 or 150 × 150 mm^2 and a matrix size of 512 × 512 pixels or 1024 × 1024 pixels, respectively. Images were reconstructed using vascular kernels of 8 sharpness levels (Bv40, Bv44, Bv56, Bv60, Bv64, Bv72, Bv80, and Bv89), using quantum iterative reconstruction (QIR) at a strength level of 4, and a slice thickness of 0.2 mm. Images with the Bv40 kernel, QIR at a strength level of 4, and a slice thickness of 0.6 mm served as the reference. Image noise, signal-to-noise ratio (SNR), contrast-to-noise ratio (CNR), vessel sharpness, and blooming artifacts were quantified. For subjective image quality, 2 blinded readers evaluated image noise and delineation of coronary artery plaques and the adjacent vessel lumen using a 5-point discrete visual scale. A phantom scan served to characterize image noise texture by calculating the noise power spectrum for every reconstruction kernel.

Results: Maximum spatial frequency (f_{peak}) gradually shifted to higher values for reconstructions with the Bv40 to Bv64 kernel (0.15 to 0.56 mm^{-1}), but not for reconstructions with the Bv72 to Bv89 kernel. Ultra-high-resolution CCTA was feasible in all patients (median calcium score, 479). In patients, reconstructions with the Bv40 kernel and a slice thickness of 0.6 mm showed largest blooming artifacts (55.2% ± 9.8%) and lowest vessel sharpness (477.1 ± 73.6 ΔHU/mm) while achieving highest SNR (27.4 ± 5.6) and CNR (32.9 ± 6.6) and lowest noise (17.1 ± 2.2 HU). Considering reconstructions with a slice thickness of 0.2 mm, image noise, SNR, CNR, vessel sharpness, and blooming artifacts significantly differed across kernels (all P's < 0.001). With higher kernel sharpness, SNR and CNR continuously decreased, whereas image noise and vessel sharpness increased, with highest sharpness for the Bv89 kernel (2383.4 ± 787.1 ΔHU/mm). Blooming artifacts continuously decreased for reconstructions with the Bv40 (slice thickness, 0.2 mm; 52.8% ± 9.2%) to the Bv72 kernel (39.7% ± 9.1%). Subjective noise was perceived by both readers in agreement with the objective measurements. Considering delineation of coronary artery plaques and the adjacent vessel lumen, reconstructions with the Bv64 and Bv72 kernel (for both, median score of 5) were favored by the readers providing an excellent anatomic delineation of plaque characteristics and vessel lumen.

Conclusions: Ultra-high-resolution CCTA with PCD-CT is feasible and enables the visualization of calcified coronaries with an excellent image quality, high sharpness, and reduced blooming. Coronary plaque characterization and delineation of the adjacent vessel lumen are possible with an optimal quality using Bv64 kernel, a FOV of 200 × 200 mm^2, and a matrix size of 512 × 512 pixels.

Key Words: photon-counting computed tomography, coronary CT angiography, ultra-high-resolution

(*Invest Radiol* 2022;57: 780–788)

Coronary artery computed tomography angiography (CCTA) has become an integral part of the diagnostic workup of patients with suspected coronary artery disease,[1,2] which is due to the excellent sensitivity and negative predictive value for the diagnosis and exclusion of coronary artery stenosis.[3] However, in patients with a high coronary calcium burden, the delineation of the luminal stenosis may be inaccurate in the presence of severe calcifications. Calcium blooming may lead to an overestimation of the stenosis grade and hence, to false-positive diagnoses in CT.[4] Increasing the spatial resolution of CT image data acquisition, hereby reducing partial volume effects of high attenuating structures, has shown to be one major technique to reduce this shortcoming.[5]

In energy-integrating detector CT (EID-CT), incident photons are indirectly converted into electrical signals. X-ray photons are first transformed into visible light by a scintillator and subsequently transduced into an electrical signal by a photodiode. To prevent optical crosstalk, optically opaque collimator blades are necessary between the EIDs, deteriorating geometric dose efficiency.[6] Acquisition of ultra-high-resolution scans with EID-CT is hampered as detector pixel is the major factor limiting spatial resolution. Hence, additional techniques such as the use of attenuating comb filters reducing the detector aperture are necessary to improve spatial resolution.[7]

Recently, the first whole-body full FOV dual-source photon-counting detector CT (PCD-CT) system has been introduced, which includes semiconducting detector elements capable of a direct conversion of incident photons to electrical signals. Absorbed x-ray photons eventually induce electron-hole pairs in the semiconductor material, with the electrons immediately attracted to the pixelated anode by the strong voltage applied across the semiconductor. As detector cells are defined by the strong electric fields, there is no need for additional separation layers, thus optimizing geometric dose efficiency and allowing smaller detector sizes.[6,8–12] With this scanner, an ultra-high-resolution mode is

Received for publication April 11, 2022; and accepted for publication, after revision, May 11, 2022.

From the *Institute of Diagnostic and Interventional Radiology, University Hospital Zurich, University of Zurich, Zurich, Switzerland; †Department of Radiology and Nuclear Medicine, Maastricht University Medical Center; ‡Cardiovascular Research Institute Maastricht, Maastricht University, Maastricht, the Netherlands; and §Siemens Healthcare GmbH, Forchheim, Germany.

Conflicts of interest and sources of funding: M.B.-B., B.S., and M.P. are employees of Siemens Healthcare GmbH. The remaining authors declare that the research was conducted in the absence of any commercial or financial relationships that could be construed as a potential conflict of interest. V.M. is funded by a research grant of the Promedica Foundation.

Correspondence to: Hatem Alkadhi, MD, MPH, EBCR, FESER, Institute of Diagnostic and Interventional Radiology, University Hospital Zurich, University of Zurich, Raemistrasse 100, CH-8091 Zurich, Switzerland. E-mail: hatem.alkadhi@usz.ch.

Supplemental digital contents are available for this article. Direct URL citations appear in the printed text and are provided in the HTML and PDF versions of this article on the journal's Web site (www.investigativeradiology.com).

ISSN: 0020-9996/22/5712–0780
DOI: 10.1097/RLI.0000000000000897

available with detector pixels of size 0.151 × 0.176 mm^2 at the isocenter.[13] This translates to a maximum spatial in-plane image resolution of 0.11 mm and a maximum through-plane resolution of 0.16 mm.

Previous phantom studies using a high-resolution mode with a prototype PCD-CT system yielded superior coronary plaque and in-stent visualization as compared with EID-CT.[14–16] High-resolution CCTA acquired with another prototype PCD-CT also outperformed EID-CT in patients with regard to overall image quality and diagnostic quality of coronary calcifications, stents, and noncalcified plaques.[17,18]

The purpose of this study was to evaluate the feasibility and quality of ultra-high-resolution CCTA with dual-source PCD-CT in patients with a high coronary calcium load, including an analysis of the optimal reconstruction kernel and matrix size.

MATERIALS AND METHODS

Phantom

A water-filled cylindrical container with 30-cm diameter was scanned using the same ultra-high-resolution PCD-CT protocol as used in the patients (see protocol details below). Following previous recommendations,[19] the noise power spectrum (NPS) of the phantom was measured to characterize image noise texture.

Patients

Consecutive patients who underwent PCD-CT with an ultra-high-resolution protocol before transcatheter aortic valve replacement within a nationwide prospective TAVR registry were screened (clinicalTrials.gov Identifier: NCT01368250). This single-center study had local ethics committee approval and was performed in compliance with the declaration of Helsinki. Written informed consent was obtained from all patients. Patients with aortocoronary bypass grafts were excluded.

CT Data Acquisition

Patient and phantom scans were performed on a first-generation, whole-body, dual-source PCD-CT system (NAEOTOM Alpha; version syngo CT VA50; Siemens Healthcare GmbH; Forchheim, Germany) equipped with 2 cadmium telluride detectors. The patient scan protocol consisted of an unenhanced scan followed by an ultra-high-resolution CCTA and subsequent CT aortography. Before the examination, patients received sublingual nitroglycerin (2.5 mg isosorbide dinitrate) if not contraindicated. No β-blocker medication for heart rate control was administered.

Ultra-high-resolution CCTA was performed using a retrospectively electrocardiography (ECG)-gated dual-source helical mode with a tube voltage of 120 kV and a collimation of 120 × 0.2 mm. Tube current-time product was adjusted to an image quality (IQ) level of 64 using automated tube current modulation, corresponding to the default protocol on the scanner. The pitch factor was automatically selected by the scanner depending on the heart rate and ranged between 0.19 and 0.32. Gantry rotation time was 0.25 seconds achieving a temporal resolution of 66 milliseconds. A total of 50 to 80 mL iodinated contrast medium (iopromide, Ultravist 370 mg iodine/mL; Bayer Healthcare, Berlin, Germany), depending on the body weight of the patients, followed by a saline chaser (NaCl 0.9%) of 20 mL applying a weight-based flow rate (3.3–4.4 mL/s) was injected into an antecubital vein using an 18-gauge catheter. Bolus tracking in the ascending aorta with a threshold of 140 HU at 90 kV was used to initiate the scan start. The ECG-pulsing window was set at fixed 30% to 80% of the R-R interval. In the ultra-high-resolution mode, detector pixels are read out separately, and the whole spectrum of absorbed photons is used employing a single energy threshold at 20 keV.[20]

Image Reconstruction

Ultra-high-resolution CCTA images were reconstructed using the following vascular kernels of 8 sharpness levels: Bv40, Bv44, Bv56, Bv60, Bv64, Bv72, Bv80, and Bv89. The % R-R phase with least motion artifacts was selected for each patient individually and was reconstructed at a slice thickness of 0.2 mm, increment of 0.2 mm, and using a novel quantum iterative reconstruction (QIR) algorithm[21] at a strength level of 4. In addition, ultra-high-resolution CCTA images were reconstructed at a slice thickness of 0.6 mm, increment of 0.3 mm, and using the Bv40 kernel and QIR at strength level of 4; these images serving as the reference standard.

The maximum spatial frequency ($\rho_{\max}$) that can be displayed in reconstructed CT images is determined by the FOV and the matrix size and can be approximated by the following equation, which is based on the Nyquist theorem[22]:

$$\rho_{max} = 1/(2 \times FOV\ [cm]/matrix\ size\ [pixels])$$

Thus, a FOV of 200 × 200 mm^2 and a matrix size of 512 × 512 pixels can display a maximum spatial frequency of $\rho_{max} = 12.8$ *line pairs* (*lp*)/*cm*. The ρ_{10} value represents an approximate measure for the maximum spatial frequency achieved by the reconstruction kernel and is defined as the frequency at which the modulation transfer function (MTF) value drops to 10% of its value at $\rho = 0$ *lp*/*cm*.[15] Table 1 lists the ρ_{10} values, FOVs, matrix sizes, and the maximum spatial frequency $\rho_{\max}$ that can be displayed for a given FOV and matrix size. It should be noted that the matrix size and FOV must be carefully adjusted, taking into account the ρ_{10} value of the reconstruction kernel to achieve optimal image quality.

In general, $\rho_{\max}$ should not be considerably lower than the ρ_{10} value of the reconstruction kernel. Otherwise, some spatial resolution provided by the reconstruction kernel will be lost due to the limited resolution capabilities of the reconstructed images. Thus, FOV and matrix size were chosen so that ρ_{max} was superior to ρ_{10} (see Table 1). Only for

TABLE 1. Reconstruction Parameters and Kernels

Kernel	ρ_{10}, Lp/cm	Field of View, mm^2	Image Matrix, Pixels	Maximum Image Resolution ($\rho_{\max}$), Lp/cm
Bv40	6.6	200 × 200	512 × 512	12.8
Bv44	7.7	200 × 200	512 × 512	12.8
Bv56	10.8	200 × 200	512 × 512	12.8
Bv60	11.8	200 × 200	512 × 512	12.8
Bv64	11.2	200 × 200	512 × 512	12.8
Bv72	17.4	200 × 200	1024 × 1024	25.6
Bv80	25.9	200 × 200	1024 × 1024	25.6
Bv89	35.9	150 × 150	1024 × 1024	34.1

Lp indicates line pairs; ρ_{10} indicates spatial frequency at which the modulation transfer function (MTF) value drops to 10% of its value at $\rho = 0$ *lp*/*cm*. The maximum image resolution $\rho_{\max}$ refers to the maximum frequency that can be displayed at a given image matrix size and field of view.

the sharpest Bv89 kernel, ρ_{max} was slightly lower than the ρ_{10} value, due to the limitation of a maximum matrix size of 1024 × 1024 pixels.

Quantitative Analysis

Phantom

The NPS was calculated for every reconstruction kernel listed previously by placing quadratic regions of interest (ROIs) in the homogenous center of the water phantom. One-dimensional NPS profiles were computed by the radial average of the 2-dimensional NPS curves. The maximum spatial frequencies of the NPS (f_{peak}) were extracted to compare the noise textures of the 8 reconstruction kernels. To reduce the complexity of the analysis, a FOV of 150 × 150 mm^2 and a matrix size of 1024 × 1024 pixels were used for all reconstructions. This is justified by the fact that with these settings ρ_{max} was superior to the ρ_{10} value for all reconstruction kernels assessed, except for the Bv89 kernel. Measurements were performed with an open-source software (ImQuest Version 7; Duke University).

Patients

Image noise, signal-to-noise ratio (SNR), and contrast-to-noise ratio (CNR) were measured by one reader V.M., resident, 3 years of experience in cardiovascular imaging. Regions of interest were placed in the aortic lumen at the level of the origin of the left main coronary artery and in the epicardial adipose tissue (EAT). Both ROIs were placed on the same image slice and chosen as large as possible, while carefully avoiding adjacent structures. Regions of interest were copied to all reconstructions using the copy-paste function. Image noise was defined as the standard deviation of attenuation measured in the ROIs placed in the ascending aorta. Signal-to-noise ratio and CNR were calculated as follows:

$$\mathrm{SNR} = \frac{\mathrm{HU_{Aorta}}}{SD_{Aorta}} \text{ and } \mathrm{CNR} = \frac{\mathrm{HU_{Aorta}} - \mathrm{HU_{EAT}}}{SD_{Aorta}}$$

HU_{Aorta} and SD_{Aorta} refer to the attenuation and the standard deviation of attenuation in the ROI placed in the ascending aorta, respectively. HU_{EAT} refers to the attenuation of the ROI placed in the EAT.

Furthermore, objective measurements of vessel sharpness and blooming artifacts were computed. For vessel sharpness, 1 reader T.S., MD-PhD student generated line profiles perpendicular to the left anterior descending artery using the "line profile" function of the open-source software FIJI[15,23] in the first 12 patients of the study. Maximum slopes of the regression lines for the anterior and posterior vessel border were calculated and averaged by computing the derivative of the line profile function using a custom in-house developed R script. This value served as a parameter for image sharpness at the vessel borders (Supplementary Fig. 1, http://links.lww.com/RLI/A724). Blooming artifacts of calcified plaques were quantified applying a previously described method.[17] In brief, 1 reader V.M. selected 1 calcified plaque and performed linear measurements of the maximal external plaque diameter and internal lumen diameter on long axis views using manual double-oblique reconstructions (Supplementary Fig. 2, http://links.lww.com/RLI/A725). Window level corresponded to the attenuation measured in the aortic lumen at the level of the origin of the left main coronary artery, and window width was obtained by multiplying the window level by 2.5. Blooming artifacts were subsequently approximated using the following formula:

$$\textit{Blooming artifact} = \frac{\textit{External calcified plaque diameter} - \textit{Lumen diameter}}{\textit{External calcified plaque diameter}} \times 100$$

Qualitative Analysis

Subjective image quality in the patients was assessed in a side-by-side comparison by 2 other, independent readers (reader 1: M.E., board-certified radiologist, 9 years of experience in cardiovascular imaging, and reader 2: H.A., board-certified radiologist, 15 years of experience in cardiovascular imaging). Readers were blinded to the kernel, FOV, and matrix sizes. Images were initially presented at predefined window settings (width, 1000 HU; level, 250 HU), and manual adjustments at the discretion of the readers were allowed.

Subjective image noise and delineation of coronary artery plaques and adjacent vessel lumen were analyzed using 5-point discrete visual scales each.

Subjective image noise was evaluated as follows: score 5 = no pixilation; 4 = minor pixilation not affecting diagnostic confidence; 3 = moderate pixilation mildly limiting diagnostic confidence; 2 = elevated pixilation reducing diagnostic confidence; and score 1 = major pixilation with poor diagnostic confidence.

Coronary artery plaques and adjacent vessel lumen were analyzed as previously shown[17]: score 5 = excellent visualization of the plaques with no perceivable blooming and precise visualization of the adjacent coronary vessel lumen; 4 = good and above average plaque and vessel lumen visualization; 3 = acceptable plaque and vessel lumen visualization; 2 = suboptimal; and score 1 = unacceptable plaque and vessel lumen visualization.

Statistical Analysis

Analyses were performed using R statistical software (R, version 4.1.1; R Foundation for Statistical Computing, Vienna, Austria, https://www.R-project.org/). Categorical variables are presented as count and percentages. The Shapiro-Wilk test was used to test continuous variables for normal distribution. Quantitative variables were expressed as mean ± standard deviation when normally distributed and as median and interquartile range (IQR) when nonnormally distributed. Friedman test was used to check for quantitative differences between the reconstructions. Interreader agreement for the subjective image evaluation was

TABLE 2. Patient Demographics

Characteristic	All Patients (n = 20)
Sex	
Male	14 (70%)
Female	6 (30%)
Age, y	79 ± 10 (range, 63–92)
Body mass index, kg/m^2	25.6 ± 4.3 (range, 17.6–33.3)
Blood pressure, mm Hg	
Systolic	147 ± 28 (range, 107–206)
Diastolic	77 ± 13 (range, 48–100)
Heart rate during the scan, bpm	76 ± 11 (range, 59–95)
Coronary artery calcium score* †	479 (251–834)
Coronary artery calcium volume, mm^3* †	453 (233–725)
Medical history	
Hypertension	16/20 (80%)
Dyslipidemia	10/20 (50%)
Diabetes	4/20 (20%)
Smoking	10/20 (50%)
Chronic obstructive pulmonary disease	3/20 (15%)
Chronic kidney disease	6/20 (30%)

Unless otherwise specified, data are mean ± standard deviation.

*Coronary artery calcium score and volume were determined using the true noncontrast scans.

†Data are medians, with interquartile ranges in parentheses.

N, number of patients, bpm = beats per minute.

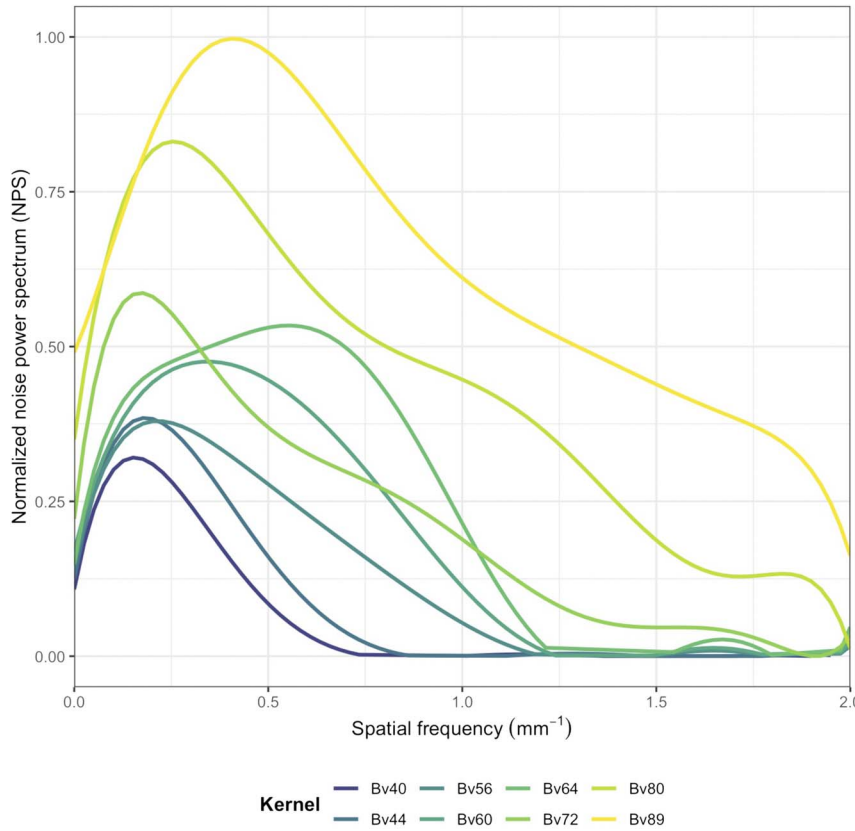

FIGURE 1. Curves depict the normalized noise power spectrum (NPS) for the different kernels assessed in the phantom scan. Note the gradual shift toward higher peak spatial frequencies for reconstructions with the Bv40, Bv44, Bv56, Bv60, and Bv64 kernel. For reconstructions with the Bv72, Bv80, and Bv89 kernel, quantum iterative reconstruction (QIR) algorithm has a pronounced effect on noise reduction in the high frequency range seen, which manifests as a strong drop toward higher frequencies.

quantified with the Krippendorff α coefficients (0, no agreement; 1, perfect agreement). Friedman tests and Wilcoxon signed rank post hoc tests were used to assess differences in the subjective analyses. The Benjamini-Hochberg procedure was used to adjust P values for multiple comparisons. A two-tailed P value below 0.05 was considered to indicate statistical significance.

RESULTS

Twenty-two eligible patients who underwent ultra-high-resolution CCTA were identified. Two patients with aortocoronary bypass grafts were excluded. Thus, 20 patients (6 women, 14 men; mean age, 79 ± 10 years; mean body mass index, 25.6 ± 4.3 kg/m^2) were finally included in this study (Table 2). Median coronary artery calcium score was 479 (interquartile range, 251–834). One patient had atrial fibrillation during scan acquisition, whereas all other patients were in sinus rhythm. Mean heart rate during data acquisition was 76 ± 11 beats per minute. Ultra-high-resolution CCTA was feasible in all patients. Mean scan time was 8.9 ± 2.0 seconds; the mean $CTDI_{vol}$ was 38.2 ± 11.1 mGy.

Quantitative Analysis

Phantom

Figure 1 shows the NPS curves of all reconstruction kernels used in this study. The maximum frequency of the NPS (f_{peak}) gradually shifted to higher values for reconstructions with the Bv40 up to the Bv64 kernel, that is, 0.15, 0.18, 0.23, 0.35, and 0.56 mm^{-1} for reconstructions with the Bv40, Bv44, Bv56, Bv60, and Bv64 kernel, respectively. There was no further shift of f_{peak} toward higher frequencies for the Bv72, Bv80 and Bv89 kernels (f_{peak} 0.18, 0.25, 0.41 mm^{-1}, respectively).

Patients

Reconstructions with the Bv40 kernel and slice thickness of 0.6 mm showed higher SNR (27.4 ± 5.6 vs 18.7 ± 3.8) and CNR (32.9 ± 6.6 vs 22.5 ± 4.5), lower image noise (17.1 ± 2.2 HU vs 25.2 ± 3.3 HU), lower vessel sharpness (477.1 ± 73.6 ΔHU/mm vs 489.7 ± 76.4 ΔHU/mm), and larger blooming artifacts (55.2% ± 9.8% vs 52.8% ± 9.2%) as compared with the Bv40 kernel and slice thickness of 0.2 mm (Fig. 2, Table 3).

Considering reconstructions with a slice thickness of 0.2 mm, image noise, SNR, CNR, vessel sharpness, and blooming artifacts significantly differed across all kernels (for all, $P < 0.001$). With higher kernel sharpness, SNR and CNR continuously diminished, whereas image noise and vessel sharpness augmented. Reconstructions with the Bv40 kernel had the lowest image noise (25.2 ± 3.3 HU), highest SNR (18.7 ± 3.8), and highest CNR (22.5 ± 4.5) but were associated with the lowest vessel sharpness (489.7 ± 76.4 ΔHU/mm). At the other extreme, reconstructions with the Bv89 kernel showed the highest vessel sharpness (2383.4 ± 787.1 ΔHU/mm) and had the highest image noise (188.8 ± 15.1 HU), lowest SNR (2.4 ± 0.4), and lowest CNR (3.0 ± 0.4). Blooming artifacts continuously decreased from reconstructions with the Bv40 kernel (52.8% ± 9.2%) to those with the Bv72

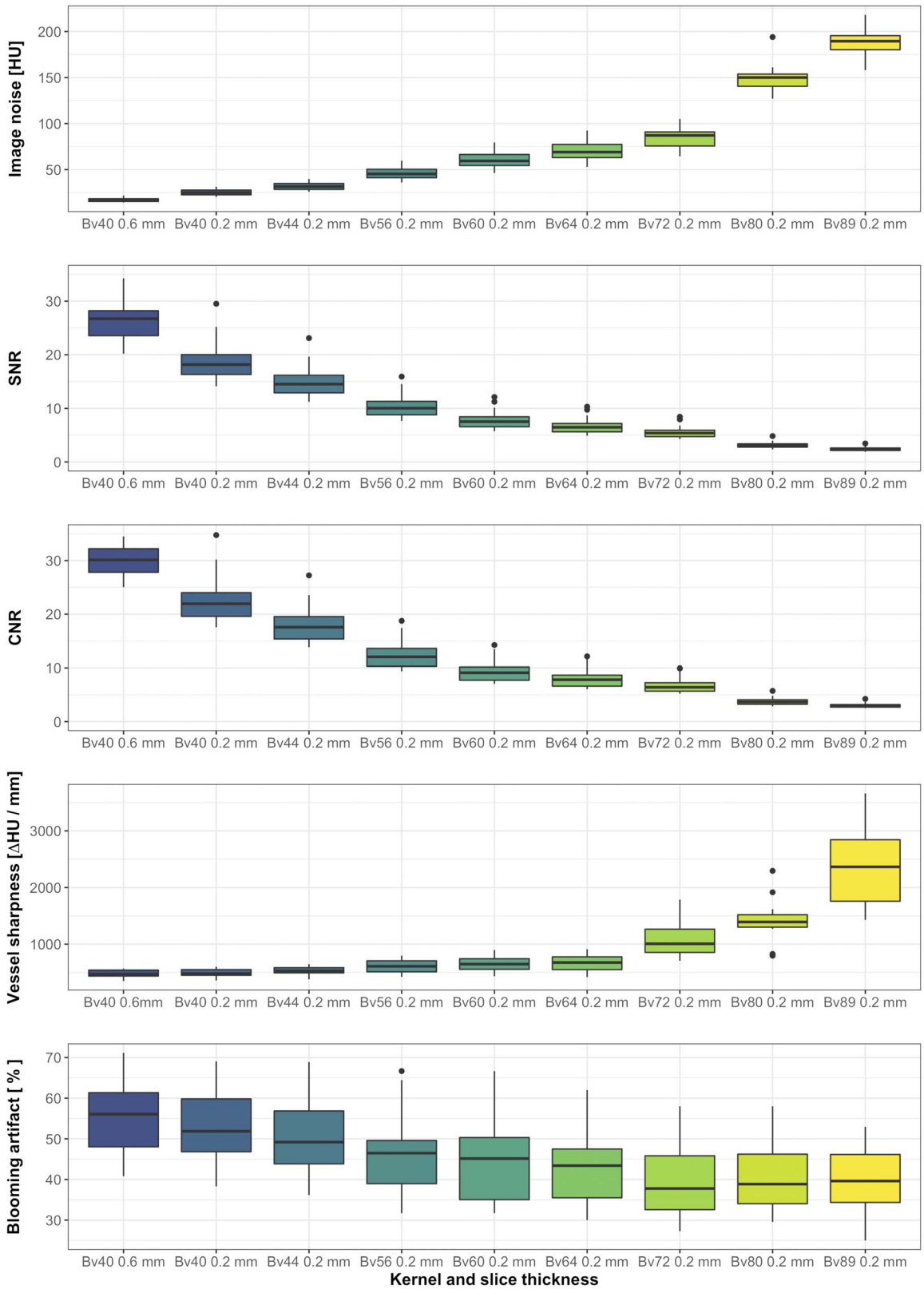

FIGURE 2. Boxplots showing measurements of the image noise, signal-to-noise ratio (SNR), contrast-to-noise ratio (CNR), vessel sharpness, and blooming artifacts of ultra-high-resolution CCTA (slice thickness, 0.2 mm) with PCD-CT in patients. Horizontal lines in the boxes correspond to the median. The top and bottom lines of the boxes correspond to the first and third quartiles, respectively. The whiskers show lowest and highest values within 1.5 interquartile range (IQR) of the lower and upper limits. Circles show outliers.

TABLE 3. Quantitative Results of Patient Scans

	Kernel and Slice Thickness								
	Bv40 0.6 mm	**Bv40 0.2 mm**	**Bv44 0.2 mm**	**Bv56 0.2 mm**	**Bv60 0.2 mm**	**Bv64 0.2 mm**	**Bv72 0.2 mm**	**Bv80 0.2 mm**	**Bv89 0.2 mm**
Image noise, HU	17.1 ± 2.2	25.2 ± 3.3	31.5 ± 4.2	46.0 ± 6.2	60.7 ± 8.5	70.6 ± 9.9	84.2 ± 10.2	148.7 ± 14.5	188.8 ± 15.1
SNR	27.4 ± 5.6	18.7 ± 3.8	14.9 ± 3.0	10.4 ± 2.2	7.9 ± 1.7	6.7 ± 1.5	5.6 ± 1.1	3.1 ± 0.6	2.4 ± 0.4
CNR	32.9 ± 6.6	22.5 ± 4.5	17.9 ± 3.6	12.5 ± 2.6	9.4 ± 2.0	8.1 ± 1.8	6.7 ± 1.3	3.8 ± 0.7	3.0 ± 0.4
Vessel sharpness, ΔHU/mm	477.1 ± 73.6	489.7 ± 76.4	528.6 ± 78.8	613.2 ± 125.3	651.2 ± 148.3	665.0 ± 152.6	1124.1 ± 370.3	1424.5 ± 408.4	2383.4 ± 787.1
Blooming artifact, %	55.2 ± 9.8	52.8 ± 9.2	50.8 ± 9.4	46.6 ± 9.8	45.1 ± 9.7	43.2 ± 9.2	39.7 ± 9.1	40.8 ± 8.4	40.4 ± 7.9

Data are mean ± standard deviation.

SNR, signal-to-noise ratio; CNR, contrast-to-noise ratio; HU, Hounsfield units.

kernel (39.7% ± 9.1%) but did not further improve using the Bv80 (40.8% ± 8.4%) or Bv89 kernel (40.4% ± 7.9%) (Supplementary Table 1, http://links.lww.com/RLI/A726).

Qualitative Analysis

Interreader agreement was nearly perfect for image noise ($\alpha = 0.88$) and for delineation of coronary artery plaques and adjacent vessel lumen ($\alpha = 0.82$). Detailed results of the subjective image quality readings are provided in Table 4.

Image noise was rated best by both readers for reconstructions with the Bv40 kernel and a slice thickness of 0.6 mm and 0.2 mm, respectively (both, 5, IQR 5–5). There were no significant differences between reconstructions with Bv40 (slice thickness, 0.6 mm and 0.2 mm, respectively) and Bv44 kernel (slice thickness, 0.2 mm; 5, IQR 5–5; for reader 1 and 5, IQR 4–5; for reader 2, all *P*'s = 0.15) for both readers. Moreover, image noise did not significantly differ between reconstructions with Bv56 (4, IQR 4–4) and Bv60 (4, IQR 4–4; $P = 0.08$) for reader 1, and between Bv44 (5, IQR 4–5) and Bv56 (5, IQR 4–5; $P = 0.14$) as well as Bv60 (4, IQR 4–4) and Bv64 (4, IQR 3–4; $P = 0.08$) for reader 2.

For delineation of coronary artery plaques and adjacent vessel lumen, highest scores were given for reconstructions with the Bv64 kernel (score 5 indicating excellent quality, IQR 5–5) for reader 1 and with the Bv72 kernel (5, IQR 5–5) for reader 2. There were no significant differences to the reconstructions with the Bv60 (5, IQR 5–5; $P = 0.39$) and Bv72 kernel (5, IQR 4–5; $P = 0.21$) for reader 1 and with the Bv60 (4, IQR 4–5; $P = 0.33$) and Bv64 kernel (5, IQR 5–5; $P = 0.78$) for reader 2.

Representative examples of ultra-high-resolution CCTA images reconstructed with different kernels, FOV, and matrix sizes showing vessel segments with calcified coronary plaques are provided in Figures 3 to 5.

DISCUSSION

Delineation of small vessel lumen with CT may be hampered by the presence of extensive vessel wall calcifications due to calcium blooming. The recently introduced PCD-CT enables the acquisition of ultra-high-resolution images with a maximum in-plane resolution of 0.11×0.11 mm^2 and a maximum through-plane resolution of 0.16 mm. This study evaluated the quality of CCTA images acquired with this ultra-high-resolution scan mode including an analysis of the optimal reconstruction kernel, FOV, and matrix size in patients with a high coronary calcium load.

In patients, ultra-high-resolution CCTA was feasible and provided high-quality images of the coronary artery tree. Although reconstructions with the Bv40 kernel and a slice thickness of 0.6 mm showed highest SNR and CNR, as well as lowest image noise, vessel sharpness, and blooming artifacts were worst. Using a slice thickness of 0.2 mm, reconstructions with the Bv89 kernel achieved highest vessel sharpness but were outperformed by reconstructions with the Bv72 kernel considering blooming artifacts. Subjective noise was perceived by both readers in agreement with the objective measurements. Coronary artery plaques and the adjacent vessel lumen could be visualized with excellent quality when using reconstructions with a higher kernel strength (Bv64 and Bv72) and when using an appropriate FOV and matrix size.

Noise texture characterization with the phantom revealed a gradual shift to higher spatial frequencies for reconstructions with the Bv40 kernel up to the Bv64 kernel. The peak value of the NPS is related to the dominant frequency in image noise, and therefore image noise texture gets finer as the kernel sharpness is increased. However, for the

TABLE 4. Qualitative Results of Patient Scans

		Kernel and Slice Thickness								
		Bv40 0.6 mm	**Bv40 0.2 mm**	**Bv44 0.2 mm**	**Bv56 0.2 mm**	**Bv60 0.2 mm**	**Bv64 0.2 mm**	**Bv72 0.2 mm**	**Bv80 0.2 mm**	**Bv89 0.2 mm**
Noise	Reader 1	5 (5–5)	5 (5–5)	5 (5–5)	4 (4–4)	4 (4–4)	4 (3–4)	3 (3–3)	2 (2–3)	2 (2–2)
	Reader 2	5 (5–5)	5 (5–5)	5 (4–5)	5 (4–5)	4 (4–4)	4 (3–4)	3 (3–4)	3 (3–3)	2 (2–3)
Plaque and vessel delineation	Reader 1	3 (2–3)	3 (3–3)	4 (4–4)	5 (4–5)	5 (5–5)	5 (5–5)	5 (4–5)	4 (3–4)	3 (3–3)
	Reader 2	3 (2–3)	3 (3–4)	4 (3–4)	4 (4–5)	4 (4–5)	5 (5–5)	5 (5–5)	4 (4–4)	4 (3–4)

Data are presented as median qualitative image analysis scores; data in parentheses are interquartile range.

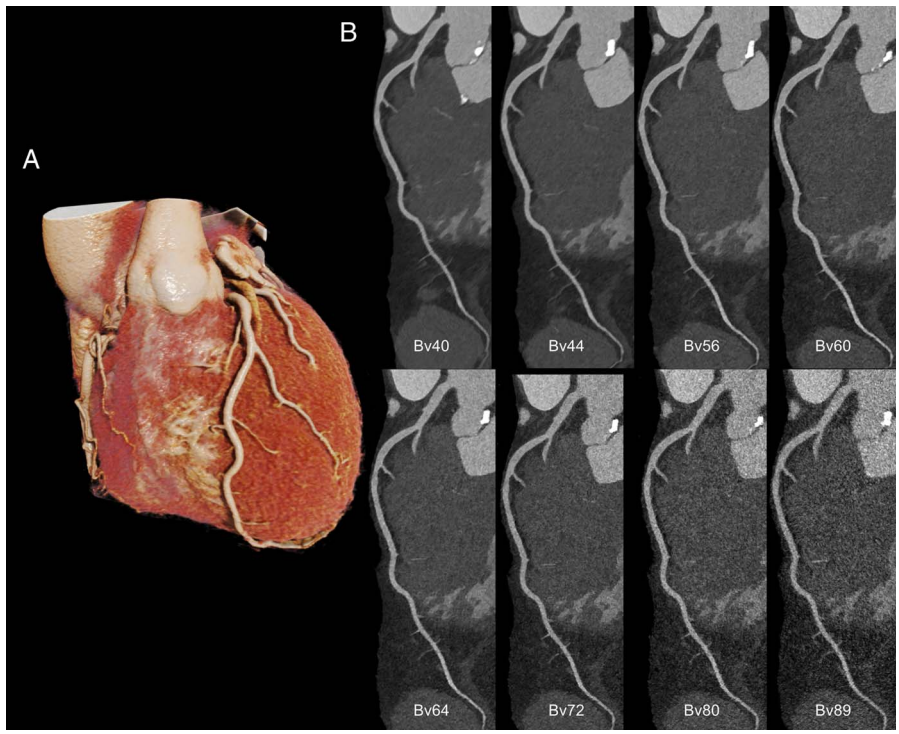

FIGURE 3. Cinematic rendering (A) and curved planar reformations (B) from ultra-high-resolution CCTA (slice thickness, 0.2 mm) with PCD-CT of the left anterior descending artery reconstructed with 8 different kernels in an 88-year-old male patient with severe aortic stenosis. Note the excellent visualization of small second-order coronary vessels across all reconstructions.

reconstructions with the Bv72, Bv80, and Bv89 kernel, spatial frequency peaked around medium values (ie, 0.18 mm^{-1} for the Bv72 kernel, 0.25 mm^{-1} for the Bv80 kernel, and 0.41 mm^{-1} for the Bv89 kernel) and showed a drop toward higher frequencies, which translates into a coarser noise texture observed in the reconstructions of the patient scans with the Bv72, Bv80, and Bv89 kernel, respectively. This strong drop is best explained by a pronounced effect of the applied iterative reconstruction algorithm at a strength level of 4 on noise reduction in the high frequency range.[21]

In our patient study, reconstructions with the Bv64 and Bv72 kernel provided an excellent anatomic visualization of plaques and

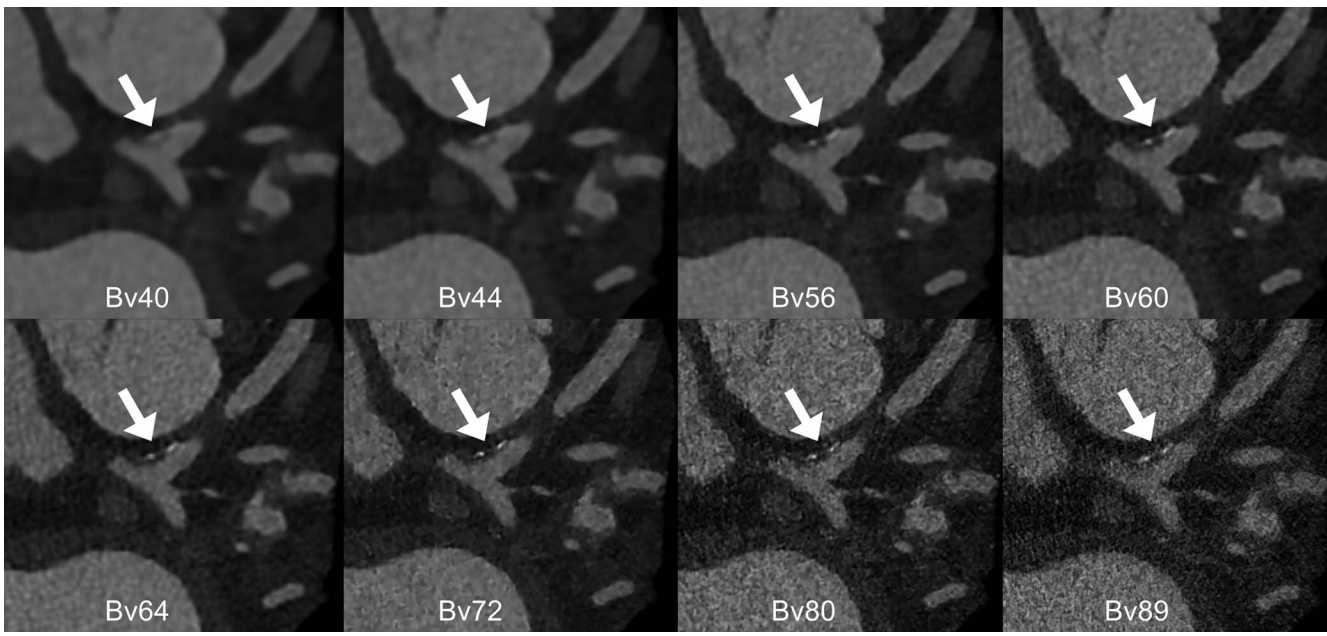

FIGURE 4. Axial images from ultra-high-resolution CCTA (slice thickness, 0.2 mm) with PCD-CT in an 88-year-old male patient with severe aortic stenosis. A mixed plaque at the distal left main to proximal left anterior descending artery is seen. Note the continuous improvement of the delineation of the partially calcified plaque at higher kernel strengths showing considerably superior anatomic detail of the small plaque.

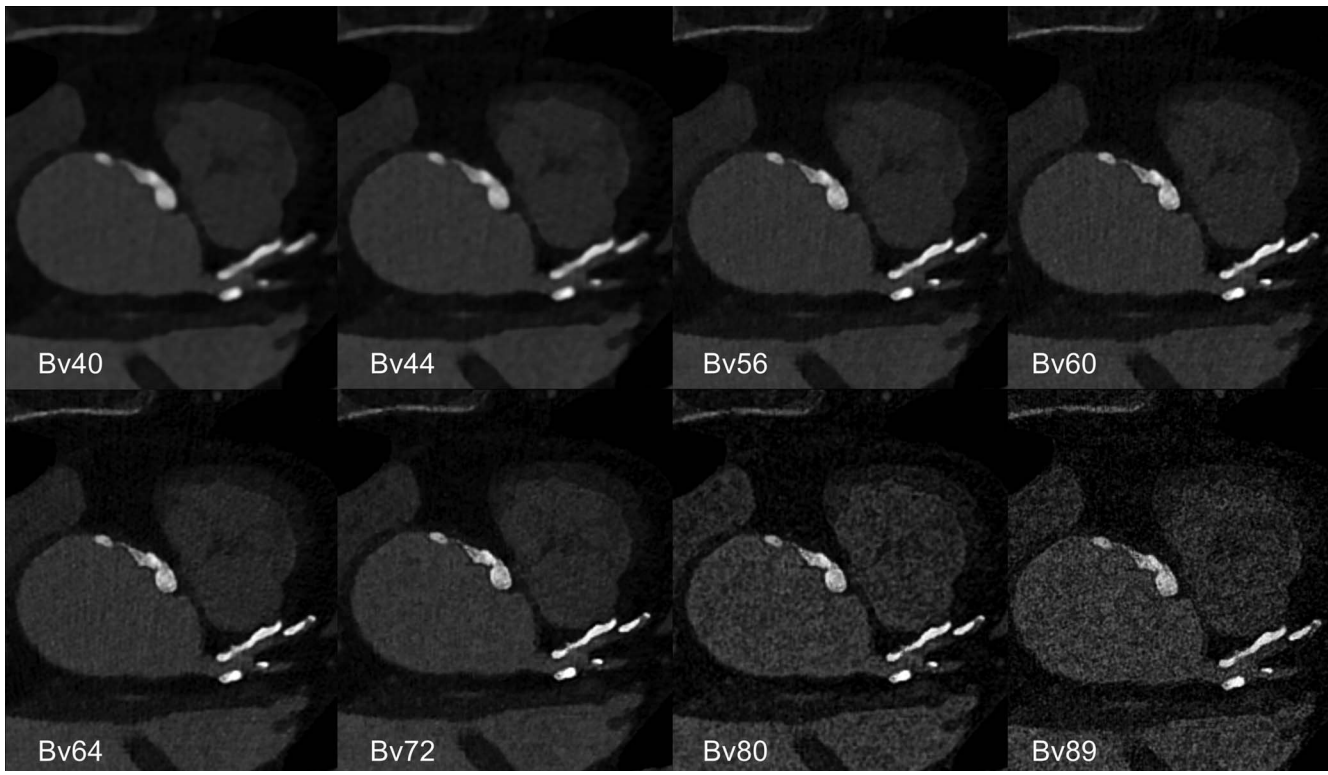

FIGURE 5. Axial images from ultra-high-resolution CCTA (slice thickness, 0.2 mm) with PCD-CT of the left main and the proximal left anterior descending artery. Although borders of calcified plaques have a blurry appearance on reconstructions with low kernel strengths, reconstructions with moderate kernel strengths (eg, Bv64) enable an excellent delineation of calcified plaques and adjacent vessel lumen before increased image noise on reconstructions with high kernel strengths (eg, Bv89) hampers vessel lumen visualization.

the adjacent vessel lumen with no perceived blooming. These findings are consistent with our results of blooming artifact quantification, yielding least blooming artifacts on reconstructions with the Bv72 kernel. Such detailed anatomic information might be clinically relevant, because there is currently great interest in the visualization of noncalcified and partially calcified coronary plaques, as these plaque types have been repetitively associated with future adverse coronary events.[24] Ultra-high-resolution CCTA with PCD-CT enabled a remarkably precise characterization of partially calcified plaques discerning noncalcified and calcified parts, potentially improving the identification of plaques prone to rupture.

Ultra-high-resolution CCTAs were acquired in dual-source helical mode with retrospective ECG-gating and a collimation of 120×0.2 mm resulting in a total z-coverage of 24 mm. This scan range resulted in an average scan acquisition time for CCTA of 8.9 ± 2.0 seconds in our patients, which is slightly longer than the acquisition time using a "standard" CCTA protocol without ultra-high-resolution. Still, all patients managed to comply with the required breath-hold time. Another issue is related to the type of ECG-gating. In this study including patients undergoing CT for planning transcatheter aortic valve replacement, a retrospectively ECG-gated dual-source spiral mode with a fixed ECG-pulsing window was used as recommended,[25] which explains our relatively high radiation dose ($CTDI_{vol}$ 38.2 ± 11.1 mGy). It is important to note that variable ECG-pulsing window settings and a sequential, prospective ECG-gated data acquisition are feasible with the ultra-high-resolution mode as well, and are the standard for CCTA to rule out coronary artery disease in patients with chronic coronary artery syndrome in our department.

Recently, Si-Mohamed et al[17] reported the image quality of CCTA applying the ultra-high-resolution parameters with a prototype PCD-CT in 14 patients, as compared with high-resolution EID-CT scans. In that study, PCD-CT outperformed EID-CT with regard to overall image quality and to the delineation of coronary calcifications, stents, and noncalcified plaques. These findings were supported by an increased detectability index for coronary lumen and noncalcified plaques in a phantom study.[17] In their study, high-resolution CCTA with the prototype PCD-CT was acquired using a collimation of 64×0.275 mm, and images were reconstructed with a section thickness and increment of 0.25 mm and 0.25 mm, respectively. The clinical PCD-CT used in our study offers superior scan and reconstruction capabilities, characterized by a collimation of 120×0.2 mm and a slice thickness of 0.2 mm.

It is important to note that no spectral information is available in the current ultra-high-resolution mode of PCD-CT,[20] whereas if CCTA is acquired with a "standard" collimation of 144×0.4 mm, the inherent spectral capabilities of PCD-CT allow for the application of various, dual-energy–based postprocessing algorithms. For example, when lumen visualization is of particular interest, blooming artifacts can be reduced by a dual-energy-based subtraction of calcified plaques (PureLumen[26]) or reconstructing virtual monoenergetic images at high energy levels.

The following study limitations merit consideration. First, patient size was limited in this single-center study. Second, accuracy of stenosis grading and plaque characterization with ultra-high-resolution CCTA was not compared with invasive catheter coronary angiography and optical coherence tomography as the standards of reference, respectively. However, we believe that the first step in evaluating a new technique must be to define the image quality and optimal reconstruction parameters before analyses of accuracy and impact on therapy and management will be conducted. Finally, ultra-high-resolution CCTA with PCD-CT was not

benchmarked to CCTA obtained with conventional EID-CT, as it is difficult to justify repeated CCTA on two different scanners in patients in a short time interval.

In conclusion, ultra-high-resolution CCTA is feasible with PCD-CT and enables the visualization of calcified coronaries with an excellent spatial resolution using dedicated sharp vascular kernels. Coronary plaque characterization and delineation of the adjacent vessel lumen is possible with an optimal quality using Bv64 kernel, a FOV of 200×200 mm^2, and a matrix size of 512×512 pixels.

REFERENCES

1. Knuuti J, Wijns W, Saraste A, et al. 2019 ESC Guidelines for the diagnosis and management of chronic coronary syndromes. *Eur Heart J*. 2020;41:407–477.
2. SCOT-HEART Investigators, Newby DE, Adamson PD, Berry C, et al. Coronary CT angiography and 5-year risk of myocardial infarction. *N Engl J Med*. 2018; 379:924–933.
3. von Ballmoos MW, Haring B, Juillerat P, et al. Meta-analysis: diagnostic performance of low-radiation-dose coronary computed tomography angiography. *Ann Intern Med*. 2011;154:413–420.
4. Song YB, Arbab-Zadeh A, Matheson MB, et al. Contemporary discrepancies of stenosis assessment by computed tomography and invasive coronary angiography. *Circ Cardiovasc Imaging*. 2019;12:e007720.
5. Latina J, Shabani M, Kapoor K, et al. Ultra-high-resolution coronary CT angiography for assessment of patients with severe coronary artery calcification: initial experience. *Radiol Cardiothorac Imaging*. 2021;3:e210053.
6. Flohr T, Petersilka M, Henning A, et al. Photon-counting CT review. *Phys Med*. 2020;79:126–136.
7. McCollough CH, Leng S, Sunnegardh J, et al. Spatial resolution improvement and dose reduction potential for inner ear CT imaging using a z-axis deconvolution technique. *Med Phys*. 2013;40:061904.
8. Leng S, Bruesewitz M, Tao S, et al. Photon-counting detector CT: system design and clinical applications of an emerging technology. *Radiographics*. 2019;39: 729–743.
9. Willemink MJ, Persson M, Pourmorteza A, et al. Photon-counting CT: technical principles and clinical prospects. *Radiology*. 2018;289:293–312.
10. Flohr T, Ulzheimer S, Petersilka M, et al. Basic principles and clinical potential of photon-counting detector CT. *Chin J Acad Radiol*. 2020;3:19–34.
11. Mergen V, Sartoretti T, Klotz E, et al. Extracellular volume quantification with cardiac late enhancement scanning using dual-source photon-counting detector CT. *Invest Radiol*. 2022;57:406–411.
12. Bratke G, Hickethier T, Bar-Ness D, et al. Spectral photon-counting computed tomography for coronary stent imaging: evaluation of the potential clinical impact for the delineation of in-stent restenosis. *Invest Radiol*. 2020;55:61–67.
13. Benson JC, Rajendran K, Lane JI, et al. A new frontier in temporal bone imaging: photon-counting detector CT demonstrates superior visualization of critical anatomic structures at reduced radiation dose. *AJNR Am J Neuroradiol*. 2022;43:579–584.
14. Rajagopal JR, Farhadi F, Richards T, et al. Evaluation of coronary plaques and stents with conventional and photon-counting CT: benefits of high-resolution photon-counting CT. *Radiol Cardiothorac Imaging*. 2021;3:e210102.
15. von Spiczak J, Mannil M, Peters B, et al. Photon counting computed tomography with dedicated sharp convolution kernels: tapping the potential of a new technology for stent imaging. *Invest Radiol*. 2018;53:486–494.
16. Mannil M, Hickethier T, von Spiczak J, et al. Photon-counting CT: high-resolution imaging of coronary stents. *Invest Radiol*. 2018;53:143–149.
17. Si-Mohamed SA, Boccalini S, Lacombe H, et al. Coronary CT angiography with photon-counting CT: first-in-human results. *Radiology*. 2022;303:303–313.
18. Boccalini S, Si-Mohamed SA, Lacombe H, et al. First in-human results of computed tomography angiography for coronary stent assessment with a spectral photon counting computed tomography. *Invest Radiol*. 2022;57:212–221.
19. International Commission on Radiation Units and Measurements. ICRU Report No. 87: radiation dose and image-quality assessment in computed tomography. *J ICRU*. 2012;12:1–149.
20. Sartoretti T, Racine D, Mergen V, et al. Quantum iterative reconstruction for low-dose ultra-high-resolution photon-counting detector CT of the lung. *Diagnostics (Basel)*. 2022;12:522.
21. Sartoretti T, Landsmann A, Nakhostin D, et al. Quantum iterative reconstruction for abdominal photon-counting detector CT improves image quality. *Radiology*. 2022;303:339–348.
22. Shannon CE. Communication in the presence of noise. *Proceedings of the IRE*. 1949;37:10–21.
23. Schindelin J, Arganda-Carreras I, Frise E, et al. Fiji: an open-source platform for biological-image analysis. *Nat Methods*. 2012;9:676–682.
24. Williams MC, Kwiecinski J, Doris M, et al. Low-attenuation noncalcified plaque on coronary computed tomography angiography predicts myocardial infarction: results from the multicenter SCOT-HEART trial (Scottish computed tomography of the HEART). *Circulation*. 2020;141:1452–1462.
25. Blanke P, Weir-McCall JR, Achenbach S, et al. Computed tomography imaging in the context of transcatheter aortic valve implantation (TAVI) / transcatheter aortic valve replacement (TAVR): an expert consensus document of the Society of Cardiovascular Computed Tomography. *J Cardiovasc Comput Tomogr*. 2019;13:1–20.
26. Allmendinger T, Nowak T, Flohr T, et al. Photon-counting detector CT-based vascular calcium removal algorithm: assessment using a cardiac motion phantom. *Invest Radiol*. 2022;57:399–405.